

Remote Sensing-Based Attribution of Urban Heat Islands to the Drivers of Heat

Fengxiang Guo^{ID}, Daniel Hertel^{ID}, Uwe Schlink^{ID}, Die Hu^{ID}, Jiangkang Qian^{ID}, and Wanben Wu^{ID}

Abstract—As cities grow and develop, more natural landscapes are transformed into heat-absorbing surfaces, further exacerbating urban heat island (UHI) effect. To seek efficient strategies for UHI mitigation, it requires a good knowledge on the driving mechanisms of heat. Based on surface energy balance (SEB), this study decomposed surface UHI (SUHI) in terms of five biophysical drivers (radiation, anthropogenic heat, convection, evapotranspiration, and heat storage) and applied the approach in Beijing using remote sensing images on Google Earth Engine (GEE). The SUHI intensity, calculated by combining the contribution terms, and the observed SUHI through Landsat 8 land surface temperature product are in good agreement, with the root-mean-square error of 0.776 K and the coefficient of determination of 0.947. Besides building morphological blocks, it is the changes of the evapotranspiration term (a function to Bowen ratio, which describes the capacity of urban and rural surface to evaporate water), that controls the spatial variations of SUHI intensity during summer. For instance, in low-rise and high-density regions that exhibit a strong SUHI effect, the above five contribution terms were 0.03, 0.44, -0.74, 1.35, and -0.08 K on average. In comparison to building height, building density strongly affects the SUHI contribution terms. Based on the results, strategies for reducing the Bowen ratio, such as green spaces, cool roofs, and open building layouts, are recommended. The findings and suggestions refer to a particular city and season. Further experiments and research should be carried out for a deeper understanding of the driving mechanism of SUHI.

Index Terms—Evapotranspiration, Google Earth Engine (GEE), remote sensing, surface energy balance (SEB), urban adaptation, urban heat island (UHI).

NOMENCLATURE

R_n	Net radiation (W/m^2).
R_n^*	Apparent net radiation (W/m^2).
Q_{AH}	Anthropogenic heat flux (W/m^2).

Manuscript received 16 December 2023; revised 19 February 2024 and 3 March 2024; accepted 11 March 2024. Date of publication 18 March 2024; date of current version 28 March 2024. This work was supported in part by the Young Scientists Fund of the National Natural Science Foundation of China under Grant 42301371 and in part by the China Postdoctoral Science Foundation under Grant 2023M730034. The work of Fengxiang Guo was supported by the China Scholarship Council under Grant 202008080124. (Corresponding author: Fengxiang Guo.)

Fengxiang Guo, Daniel Hertel, and Uwe Schlink are with the Department of Urban and Environmental Sociology, UFZ—Helmholtz Centre for Environmental Research, 04318 Leipzig, Germany (e-mail: fengxiang.guo@ufz.de; daniel.hertel@ufz.de; uwe.schlink@ufz.de).

Die Hu is with the Sino-French Institute for Earth System Science, College of Urban and Environmental Sciences, Peking University, Beijing 100871, China (e-mail: hudie@radi.ac.cn).

Jiangkang Qian is with the Aerospace Information Research Institute, Chinese Academy of Sciences, Beijing 100094, China (e-mail: qianjiangkang20@mails.ucas.ac.cn).

Wanben Wu is with the Department of Biology, Aarhus University, 8000 Aarhus, Denmark (e-mail: wanben.wu@bio.au.dk).

Digital Object Identifier 10.1109/TGRS.2024.3378287

Q_H	Sensible heat flux (W/m^2).
Q_E	Latent heat flux (W/m^2).
Q_S	Soil heat flux (W/m^2).
S_{\downarrow}	Incoming solar radiation (W/m^2).
L_{\downarrow}	Downward blackbody radiation (W/m^2).
L_{\uparrow}	Upward blackbody radiation (W/m^2).
ε_0	Surface emissivity.
ε_a	Atmospheric emissivity.
σ	Stefan Boltzmann's constant ($\text{W}/\text{m}^2/\text{K}^4$).
α	Surface albedo.
e_s	Saturated vapor pressure of air (hPa).
e_a	Vapor pressure of air (hPa).
ρ	Air density (kg/m^3).
C_p	Specific heat ($\text{J} \cdot \text{kg}^{-1} \cdot \text{K}^{-1}$).
r_a	Aerodynamic resistance (s/m).
λ	Psychrometric constant (hPa/K).
β	Bowen ratio.
T_s	Land surface temperature (K).
T_a	Air temperature (K).
$T_{s,r}$	Rural T_s (K).
$T_{s,u}$	Urban T_s (K).
μ^*	Friction velocity.
ΔT_{R_n}	Radiation term (K).
ΔT_{AH}	Anthropogenic heat term (K).
ΔT_{Con}	Convection term (K).
ΔT_{Eva}	Evapotranspiration term (K).
ΔT_{HS}	Heat storage term (K).
VEG	Vegetation zone.
LRP	Low-rise point.
LRS	Low-rise stripe.
LRB	Low-rise block.
MRP	Middle-rise point.
MRS	Middle-rise stripe.
MRB	Middle-rise block.
HRP	High-rise point.
HRS	High-rise stripe.
HRB	High-rise block.
ABF	Average building floor.
ABD	Average building density.

I. INTRODUCTION

URBAN heat island (UHI) is a common phenomenon, in that urban areas experience higher temperatures than surrounding rural areas [1], [2]. Since 2003, the surface temperature in pronounced UHI regions has risen by about 1.04 K on average around the world [3]. Elevated urban

temperatures contribute to extreme heat events, air pollution, posing threats to the health of urban dwellers, and the living conditions of flora and fauna [4], [5], [6]. Therefore, seeking an approach for UHI mitigation is necessary and urgent.

UHI studies include the analysis of air temperature and satellite-based land surface temperature (LST) [7], [8], [9], [10], [11], [12], [13], [14], [15]. The former considers the UHI effect in the canopy or boundary layers, typically measured at varying heights above the ground [12], [13]. The latter is primarily concerned with temperature variations at the ground level or within a few centimeters above the surface, which highlights the physical changes in land cover and land use (LULC) associated with urban development [9], [10], [11], [12], [13], [14], [15]. This study focused on the surface UHI (SUHI) defined by LST. Besides the advantages of spatiotemporal consistency and spatial coverage, LST is independent of conventional meteorological variables, which directly affect the surface heat budget in urban regions [15], [16], [17]. Both the air and SUHIs are controlled by multiple factors: absorbed solar radiation, released anthropogenic heat, heat storage and release at surface, geometrical features to urban ventilation, and higher Bowen ratio (defined as the ratio from sensible to latent heat flux) caused by reduced vegetation/water coverage [7], [18], [19]. Identifying vulnerable sites (often affected by heat) and developing efficient local mitigation strategies requires a comprehensive understanding of these drivers of heat. Urban heat and its biophysical drivers depend on the urban structure that can be characterized by different types of urban morphology. These relationships are essential for optimizing urban design, minimizing cost and efforts, and preventing the adverse effects of heat on urban ecosystems.

The quantification of contribution terms to UHI intensity is the key to develop targeted measures for UHI mitigation. This can be achieved through the application of surface energy balance (SEB) model [7], [18]. The SEB describes the partitioning of energy fluxes available at the surface, which forms the basis for understanding the thermodynamic behavior of air and surface temperature, humidity, local airflow dynamics, and boundary layer depth [20], [21], [22], [23]. In the absence of horizontal heat advection, the net radiation (R_n) and anthropogenic heat flux (Q_{AH}) are balanced by sensible heat flux (Q_H), latent heat flux (Q_E), and soil heat flux (Q_S) for an urban area (Fig. 1)

$$R_n + Q_{AH} = Q_H + Q_E + Q_S. \quad (1)$$

To decompose UHI intensity, Zhao et al. [7] applied the intrinsic biophysical mechanism (IBM) method in North America using SEB fluxes extracted from a global climate model (CESM) and compared the modeled UHI result with a remote sensing-based UHI. They found that the dominant contribution term of UHI intensity is different between daytime and night. During the daytime, the UHI intensity is primarily controlled by the efficiency of heat convection from the surface to the atmosphere, which in turn is dependent on climate zones. In northeastern cities of USA, the dominant term shifts to the capacity of the urban surface to evaporate water. Later, Li et al. [19] suggested a two-double resistance mechanism (TRM), which specifies a surface resistance to replace the

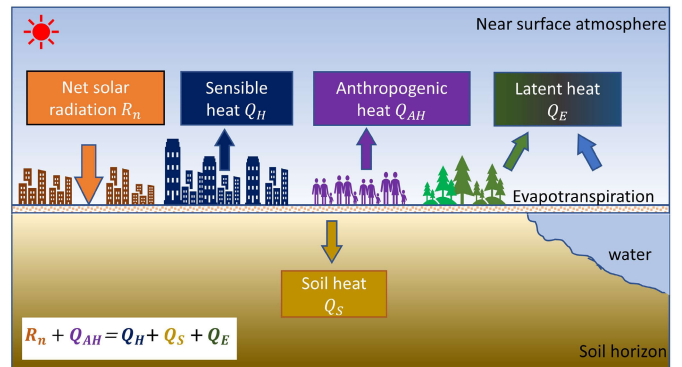


Fig. 1. Schematic depiction of terms involved in the SEB. The arrow orientation represents positive fluxes.

Bowen ratio term in IBM. The results showed some similarity to [7] but emphasize evapotranspiration as the most dominant contribution. However, these studies only discussed the UHI formation at a city scale, without addressing their spatial variations within a city. This limitation complicates the understanding of UHI driving mechanisms and the identification of vulnerable regions. To decompose UHI at the neighborhood scale, Hertel and Schlink [18] employed the IBM method using SEB fluxes obtained from micrometeorological simulations (ENVI-met) in Leipzig, Germany, but the input variables were not easy to access and the simulation takes significant time (few days), even for a modeling area of 1125×1125 m. This limits its further application, especially in metropolitan cities.

Closing these gaps, this study applied the IBM method to decompose SUHI intensity in Beijing, China, and implemented the entire process on Google Earth Engine (GEE) for a potential application in various scenarios. Compared with the traditional LULC-based analysis of SUHI, the suggested method is advantageous for quantifying the local heat transfer process and further converting them into corresponding temperature changes. This would provide new insights for future efforts to attribute UHI at a fine spatial scale and scientific guides to future urban transformation. Our specific objectives include the following:

- 1) mapping the contribution terms of SUHI intensity to facilitate the identification of vulnerable regions within Beijing;
- 2) investigating which contribution term exerts the greatest influence on SUHI intensity;
- 3) analyzing the association between each contribution term and urban morphology [urban morphological blocks (UMBs)], in order to provide scientific recommendations for UHI mitigation in Beijing.

II. STUDY AREA AND DATA

A. Study Area

Beijing ($39^{\circ}54'N$, $116^{\circ}23'E$) is a world-class city that is undergoing rapid urbanization and substantial population growth, covering approximately $16\,000 \text{ km}^2$ with more than 20 million urban populations. Situated in the north temperate climate zone, the city features a humid continental monsoon

climate characterized by harsh, dry winters, and hot summers [24]. Beijing encounters a significant UHI effect, particularly during the summer months, with the urban region often being approximately 3.5 °C warmer than its outskirts [25]. In this study, the urban region is defined as the area enclosed by the Fifth Ring Road (Fig. 2), while the suburban region encompasses all nonurban pixels within a 10-km buffer outside the urban boundary.

B. Data

In this study, Landsat 8 OLI/TIRS data from August 6, 2021, and December 4, 2018, were utilized to retrieve LST and estimate SEB fluxes. The former image was further employed to calculate SUHI contribution terms during summer in Beijing, while the latter was employed to analyze the accuracy of estimated SEB fluxes by comparison to [26]. Most of Landsat 8 bands have a spatial resolution of 30 m except thermal infrared bands (100 m) and panchromatic band (15 m). The thermal infrared bands on Landsat 8 has a spatial resolution of 100 m, but after resampling (cubic convolution method is applied on GEE), it can supply LST products using the atmosphere correction method with a spatial resolution of 30 m and an overall accuracy of 1 K [27].

NASA's Shuttle Radar Topography Mission (SRTM) data have a spatial resolution of 30 m, were applied to obtain the elevation, and further calibrate LST by transferring the difference of extraterrestrial solar radiation between fluctuated and flat terrains to the changes in temperature [23], [28].

In terms of meteorological data, we used the ERA5 hourly atmospheric reanalysis dataset to estimate the SEB fluxes from Landsat images. This dataset was chosen due to its global coverage and accessibility on GEE. It provides hourly, spatially continuous data for parameters such as air temperature at 2 m, dew-point temperature at 2 m, wind speed at 10 m, and surface solar radiation at a resolution of 0.1° since 1980 [29].

The UMBs dataset was sourced from Beijing City Lab, which provides block-scale 3-D attributes for 63 Chinese cities [30], [31]. This study collected the block data of urban region in Beijing, with nine UMB types (Table I), serving as the fundamental spatial units for an analysis of the associations with SEB fluxes and SUHI contribution terms (Fig. 2). The land cover data, employed to identify vegetation and water regions, come from the China land cover dataset (CLCD), offering a spatial resolution of 30 m and an accuracy exceeding 79.31% [32].

III. METHODS

A. Estimation of Various Heat Fluxes

1) *Net Radiation*: Net radiation (W/m^2) refers to the balance of radiation at the land surface that can be calculated using incoming shortwave radiation (S_{\downarrow}), incoming longwave radiation from the atmosphere (L_{\downarrow}), and emitted/outgoing longwave radiation from the surface (L_{\uparrow}), which is described by the following equation [23]:

$$R_n = (1 - \alpha)S_{\downarrow} + L_{\downarrow} - (1 - \varepsilon_0)L_{\downarrow} - L_{\uparrow} \quad (2)$$

TABLE I
DESCRIPTION OF UMBs CATEGORIES

UMB type	Abb.	Descriptions
Low-rise point	LRP	Low-rise and low-density region (ABF < 3 & ABD < 0.25)
Low-rise stripe	LRS	Low-rise and middle-density region (ABF < 3 & 0.25 <= ABD < 0.35)
Low-rise block	LRB	Low-rise and high-density region (ABF < 3 & 0.35 <= ABD < 0.45)
Middle-rise point	MRP	Middle-rise and low-density region (3 <= ABF <= 7 & ABD < 0.25)
Middle-rise stripe	MRS	Middle-rise and middle-density region (3 <= ABF <= 7 & 0.25 <= ABD < 0.35)
Middle-rise block	MRB	Middle-rise and high-density region (3 <= ABF <= 7 & 0.35 <= ABD < 0.45)
High-rise point	HRP	High-rise and low-density region (ABF > 7 & ABD < 0.25)
High-rise stripe	HRS	High-rise and low-density region (ABF > 7 & 0.25 <= ABD < 0.35)
High-rise block	HRB	High-rise and low-density region (ABF > 7 & 0.35 <= ABD < 0.45)

Notes: ABF means the average building floor in the region, and ABD means the average building density in the region.

where α and ε_0 represent surface albedo (dimension less) and surface emissivity (dimension less), respectively. The surface albedo can be calculated as [33]

$$\alpha = (\alpha_{\text{toa}} - \alpha_{\text{path-radiance}}) / \tau_{\text{sw}}^2 \quad (3)$$

where $\alpha_{\text{path-radiance}}$ represents the average of the part of solar incident radiance for all bands and α_{toa} represents the top-of-atmosphere albedo. The atmospheric transmissivity τ_{sw} is determined using the following equation [22]:

$$\tau_{\text{sw}} = 0.75 + 2 * 10^{-5} Z \quad (4)$$

where Z is the height of an area from the mean sea level.

The incoming shortwave radiation is processed by the following equation:

$$S_{\downarrow} = G_{\text{sc}} * \cos\theta * d_r * \tau_{\text{sw}} \quad (5)$$

where G_{sc} is the solar constant (1367W/m^2), θ is the Sun elevation angle, and d_r is the inverse square relative distance between the Earth and the Sun [22].

The incoming longwave radiation from the atmosphere (L_{\downarrow}) at every pixel is calculated using the Stefan–Boltzmann equation

$$\begin{aligned} L_{\downarrow} &= \varepsilon_a * \sigma * T_a^4 \\ \varepsilon_a &= 0.85 * (-\ln \tau_{\text{sw}})^{0.09} \end{aligned} \quad (6)$$

where ε_a is atmospheric emissivity (dimension less), σ is Stefan–Boltzmann's constant ($5.67 \times 10^{-8} \text{W/m}^2/\text{K}^4$), and T_a is the air temperature (K).

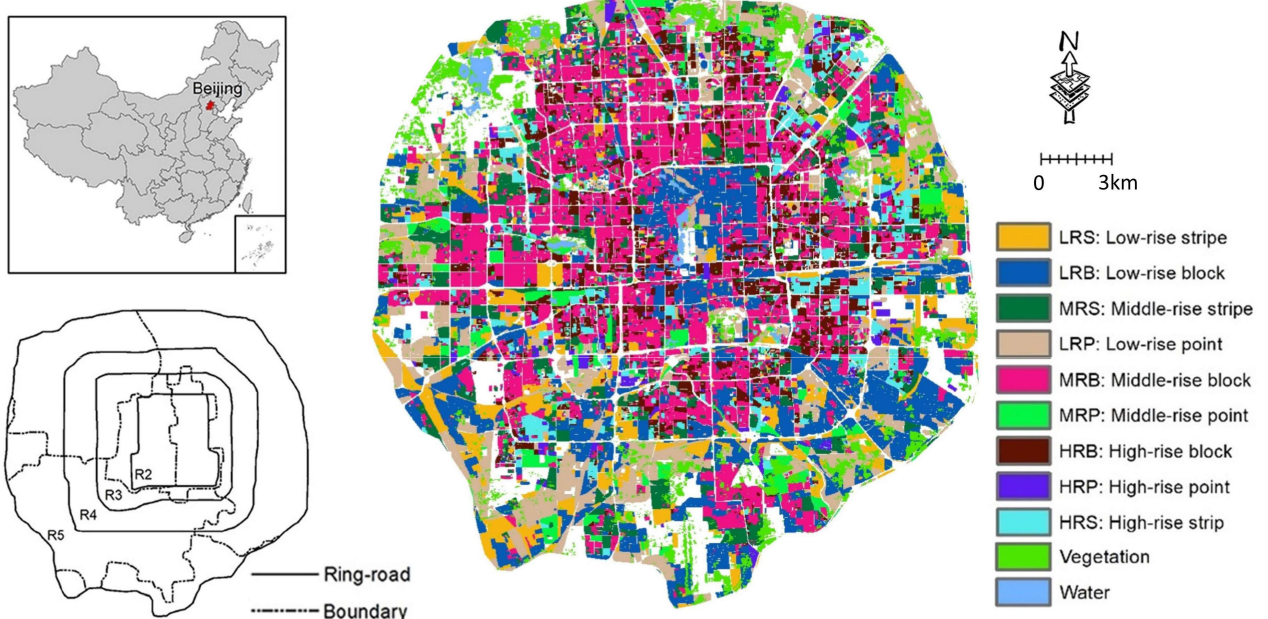


Fig. 2. Study area. (Top left) Map of China. (Bottom left) Location of main Ring Road in Beijing. (Right) Distribution of UMBs and VEG within Fifth Ring Road in Beijing.

The emitted/outgoing longwave radiation from the surface (L_{\uparrow}) is calculated using the following equation:

$$\begin{aligned} L_{\uparrow} &= \varepsilon_0 * \sigma * T_s^4 \\ \varepsilon_0 &= 1.009 + 0.047 \times \ln(\text{NDVI}) \end{aligned} \quad (7)$$

where T_s is the surface temperature (K).

2) *Sensible Heat Flux*: Sensible heat flux (W/m^2) refers to the heat transfer to the atmosphere by molecular convection due to temperature differences. When the surface temperature exceeds the air temperature, the heat transfer is upward from the surface to the atmosphere [18], [34]. The sensible heat flux is calculated using the following equation:

$$Q_H = \rho * C_p * (T_s - T_a) / r_a \quad (8)$$

where ρ is the air density (kg/m^3), C_p is the specific heat of air at constant pressure (1004 $\text{J}/\text{kg}/\text{K}$), and r_a means the aerodynamics resistance to turbulent heat transfer from surface at the reference height to the air (s/m). Since the temperature gradient dT ($T_s - T_a$) and r_a are two unknowns, sensible heat flux (Q_H) was estimated through an iterative process using (9) according to [35]. To determine dT , it is necessary to assume a linear relationship between dT and T_s

$$dT = aT_s + b \quad (9)$$

where a and b are the calibration coefficients, calculated by selecting hot and cold endmembers. For hot pixels, Q_H is assumed to be the maximum, while latent heat flux Q_E is assumed as zero. For cold pixels, Q_H is assumed to be zero, while Q_E is related to all available energy.

In the iteration process, the first estimation r_a is determined by the following equation:

$$r_a = \ln(z_2/z_1)/k\mu^* \quad (10)$$

where k is the von Karman constant (0.41), z_2 and z_1 are the heights to calculate dT (usually 2 and 0.1 m), and μ^* is the friction velocity estimated using wind speed at a blending height of 200 m and the surface roughness. For later each iteration process, r_a is corrected using an atmospheric stability correction based on the Monin–Obukhov similarity [36] until the final result reached to be stable.

3) *Latent Heat Flux*: Latent heat flux (Q_E) refers to the heat exchange between land surface and atmosphere due to evaporation of water and transpiration of vegetation, which does not cause a change in temperature [20]. Q_E is estimated using the following equation according to [37]:

$$Q_E = \rho C_p (e_s - e_a) / \lambda (r_a + r_s) \quad (11)$$

where λ is the psychrometric constant (hPa/K); r_s is the stomatal resistance (s/m) depending on the vegetation, meteorological, and atmospheric conditions; and e_s and e_a refer to the saturation and atmospheric water vapor pressure (hPa) at the surface temperature, respectively.

4) *Soil Heat Flux*: Soil heat flux (Q_S) is the heat transfer in and out of the soil by molecular convection, which can be estimated using vegetation index and net radiation [38]

$$Q_S = \left[\frac{(T_s - 273.15)}{\alpha} (0.0038\alpha + 0.0074\alpha^2) \right. \\ \left. \times (1 - 0.98\text{NDVI}^4) \right] R_n \quad (12)$$

where NDVI is the normalized differential vegetation index.

5) *Anthropogenic Heat Flux*: Here, anthropogenic heat flux (Q_{AH}) was estimated by (1) as a residual. Q_{AH} is the heat energy released into the environment due to human activities. The potential heat sources include energy consumption (e.g., industrial process and combustion engine), building energy use (e.g., eating, cooling, and electrical systems in buildings),

and transportation (e.g., combustion of fossil fuels in vehicles) [39], [40], [41].

B. SUHI Decomposition

In order to quantify the contribution of various heat fluxes to SUHI intensity, we formulated SEB following the method of [7] and [42] and decomposed SUHI intensity into different biophysical terms. We additionally calculated the contribution of anthropogenic heat term from remote sensing image

$$(1 - \alpha)S_{\downarrow} + L_{\downarrow} - L_{\uparrow} + Q_{AH} = \left(1 + \frac{1}{\beta}\right) \frac{\rho C_p}{r_a} (T_s - T_a) + Q_s \quad (13)$$

where β is the Bowen ratio, defined by Q_H/Q_E . After linearizing the outgoing longwave radiation using Taylor series, (13) can be described as

$$-4\sigma\varepsilon_0 T_a^3 (T_s - T_a) + Q_{AH} = \left(1 + \frac{1}{\beta}\right) \frac{\rho C_p}{r_a} (T_s - T_a) + Q_s. \quad (14)$$

Following [7], we define $f = (1 + (1/\beta))(\rho C_p/r_a) \lambda_0$, where $\lambda_0 = (1/4\varepsilon_0\sigma T_a^3)$. The former is an energy redistribution factor and the latter coincide with the definition of the local climate sensitivity parameter [18], [43]. A solution for T_s is obtained from (14) [19]

$$T_s - T_a = \frac{\lambda_0}{1 + f} (R_n^* + Q_{AH} - Q_s). \quad (15)$$

The urban and rural regions belonging to one city share the same background climate feature and receive the same incoming shortwave radiation. At a blending height of 200 m, the air is well blended, and therefore, T_a is the same among locations in a city [42]. We defined urban LST as $T_{s,u} = T_{s,r} + \Delta T_s$, where u and r represent urban and rural status, respectively. The parameters $R_{n,u}^*$, $Q_{AH,u}$, $Q_{s,u}$, β_u , $r_{a,u}$, and f_u have the analog definition and replacement. Equation (15) applied to the urban and rural regions yields

$$\begin{aligned} T_{s,u} - T_a &= \frac{\lambda_0}{1 + f_u} (R_{n,u}^* + Q_{AH,u} - Q_{s,u}) \\ T_{s,r} - T_a &= \frac{\lambda_0}{1 + f_r} (R_{n,r}^* + Q_{AH,r} - Q_{s,r}). \end{aligned} \quad (16)$$

Assuming small perturbations (Δ) generated by the urban structure, we can calculate the derivatives of all variables that are connected with Δ [18]. Finally, ΔT_s can be taken as SUHI intensity at different urban sites, as shown in the following equation:

$$\begin{aligned} \text{SUHI} &= T_{s,u} - T_{s,r} = \left(\frac{\lambda_0}{1 + f_r} - \frac{\lambda_0}{(1 + f_r)^2} \Delta f \right) \\ &\quad \times (R_{n,r}^* + \Delta R_{n,r}^* + Q_{AH,r} + \Delta Q_{AH} - Q_{s,r} - \Delta Q_s) \\ &\quad - \frac{\lambda_0}{1 + f_r} (R_{n,r}^* + Q_{AH,r} - Q_{s,r}) \\ &= \frac{\lambda_0}{1 + f_r} (\Delta R_{n,r}^* + \Delta Q_{AH} - \Delta Q_s) \\ &\quad - \frac{\lambda_0}{(1 + f_r)^2} \Delta f (R_{n,r}^* + \Delta R_{n,r}^* + Q_{AH,r} \\ &\quad + \Delta Q_{AH} - Q_{s,r} - \Delta Q_s). \end{aligned} \quad (17)$$

Neglecting the higher order terms $o(\Delta^2) \approx 0$ [18], [19], we obtain

$$\begin{aligned} \text{SUHI} &= \frac{\lambda_0}{1 + f_r} (\Delta R_n^* + \Delta Q_{AH} - \Delta Q_s) \\ &\quad - \frac{\lambda_0}{(1 + f_r)^2} \Delta f (R_{n,r}^* + Q_{AH,r} - Q_{s,r}) \end{aligned} \quad (18)$$

where

$$\begin{aligned} \Delta f &= f_u - f_r = \left(1 + \frac{1}{\beta_r}\right) \frac{-\lambda_0 \rho C_p}{r_{a,r}^2} \Delta r_a \\ &\quad + \frac{-\lambda_0 \rho C_p}{r_{a,r}} \frac{\Delta \beta}{\beta_r^2} \end{aligned} \quad (19)$$

with

$$\begin{aligned} \Delta f_1 &= \left(1 + \frac{1}{\beta_r}\right) \frac{-\lambda_0 \rho C_p}{r_{a,r}^2} \Delta r_a \\ \Delta f_2 &= \frac{-\lambda_0 \rho C_p}{r_{a,r}} \frac{\Delta \beta}{\beta_r^2}. \end{aligned} \quad (20)$$

Therefore, the expanded form of (18) is given as

$$\begin{aligned} \text{SUHI} &= \underbrace{\frac{\lambda_0}{1 + f_r} \Delta R_n^*}_{\text{radiation term}} + \underbrace{\frac{\lambda_0}{1 + f_r} \Delta Q_{AH}}_{\text{anthropogenic heat term}} \\ &\quad + \underbrace{\frac{-\lambda_0}{(1 + f_r)^2} (R_{n,r}^* - Q_{s,r} + Q_{AH}) \Delta f_1}_{\text{convection term}} \\ &\quad + \underbrace{\frac{-\lambda_0}{(1 + f_r)^2} (R_{n,r}^* - Q_{s,r} + Q_{AH}) \Delta f_2}_{\text{evapotranspiration term}} \\ &\quad + \underbrace{\frac{-\lambda_0}{1 + f_r} \Delta Q_s}_{\text{heat storage term}}. \end{aligned} \quad (21)$$

Finally, the SUHI intensity is decomposed into five contribution parts: radiation term (ΔT_{-R_n}), anthropogenic heat term (ΔT_{-AH}), convection term (ΔT_{-Con}), evapotranspiration term (ΔT_{-Eva}), and heat storage term (ΔT_{-HS}).

C. Accuracy Estimation

The accuracy estimation of this study compares: 1) SEB fluxes with 2) simulated SUHI intensity by adding all five SUHI contribution terms together. For 1), we only validated the anthropogenic heat flux (Q_{AH}), without others due to lack of in situ measurements from a flux tower. This study took the Q_{AH} product published by Meng et al. [26] as reference data and made a comparison with our result using the same Landsat image (on December 4, 2018). To estimate the accuracy of simulated SUHI intensity, we calculated the SUHI intensity directly from the Landsat 8 LST product, which was taken as the reference data.

IV. RESULTS

A. Validation of Anthropogenic Heat Flux and SUHI Contribution Terms

The residual map illustrated a strong consistency between the extracted Q_{AH} in this study and the reference data, with

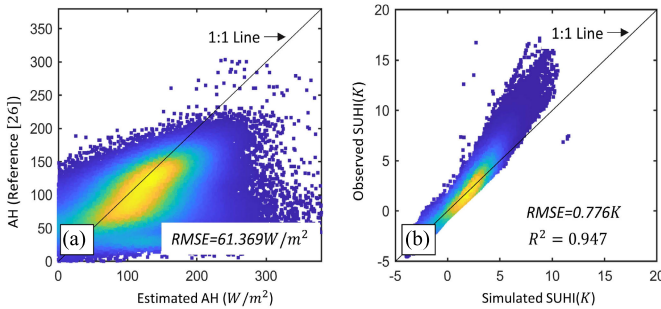


Fig. 3. Accuracy estimation. (a) Comparison between AH estimated in this study and [26]. (b) Comparison between observed and simulated SUHI on August 6, 2021.

the majority of residuals centered around 0 and an RMSE of $61.369 W/m^2$ [Fig. 3(a)]. The simulated and observed SUHI intensity predominantly align along the 1:1 line [Fig. 3(b)] and RMSE (0.776 K) and R^2 (0.947) suggest a high quality of the estimated SUHI. Note that when SUHI intensity exceeds 5 K, the observed values are obviously higher than the simulated values, suggesting an underestimate of simulated SUHI intensity in very hot regions. This is in accordance with the findings of other authors using the same method [7], [44]. The error may come from the IBM method itself, which assumes that the aerodynamics resistance was independent of Bowen ratio. This assumption is likely to cause an overestimate of convection term and an underestimate of radiation and heat storage term [19].

B. SUHI Contribution Terms and the Relationship With UMBs

The SUHI intensity during the daytime within Second Ring Road is much higher than that in outside regions, which suggested a gradual decrease in SUHI intensity with increasing distance from the urban core (Fig. 4). In Fig. 5(a), UMBs exhibit distinct SUHI phenomena, while areas with vegetation serve as urban cool islands. Fig. 5(a) also showed that SUHI intensity increased much more significantly with building density than with building height, suggesting that the influence of building density may surpass that of building height. Among UMBs, the SUHI intensity at the low-rise and high-density region (LRB) was the strongest, with a median value of around 3 K, followed by the middle-rise and high-density region (MRB) and the high-rise and high-density region (HRB).

The radiation term (ΔT_{R_n}) exhibited a similar tendency with SUHI, with higher values observed in the core urban region compared to the urban periphery (Fig. 4). Among UMBs, ΔT_{R_n} showed an increase in both building density and building height [Fig. 5(b)]. Notably, when focusing on the boxplot, it becomes evident that the high-rise region (HRP, HRS, and HRB) has a larger contribution on the SUHI intensity than the middle-rise and low-rise regions. Although the median values ΔT_{R_n} are positive, their magnitude remained quite small, nearly approaching zero.

The anthropogenic heat term (ΔT_{AH}) is prominently concentrated within the core urban region (especially within

Second Ring Road) and tended to be scattered in the outside region (Fig. 4). In addition, several locations in the southern part exhibit stronger ΔT_{AH} . Within most UMBs, ΔT_{AH} consistently registers values above 0, indicating a positive contribution to high urban temperatures [Fig. 5(c)]. The relationships between UMBs and ΔT_{AH} are quite similar to observed SUHI. The impacts of building density on ΔT_{AH} exceed that of building height. The most substantial contribution from ΔT_{AH} to SUHI intensity was observed in the LRB, and then MRB and HRB, with all median values exceeding 0.5 K. The middle-density region (LRS, MRS, and HRS) also displayed a relatively high contribution.

The convection term (ΔT_{Con}) plays a converse role in SUHI by comparison to ΔT_{AH} , as it tends to be more prominent in regions distant from the core urban regions (Fig. 4). ΔT_{Con} is directly influenced by aerodynamic resistance (r_a), as shown in (20). A higher r_a indicates more efficient heat transfer from the surface to atmosphere in an upward direction, which reduces local LST at the time of image acquisition. This effect is particularly obvious in regions with higher LST, where more sensible heat flux may be generated. Among UMBs, ΔT_{Con} appeared to be more sensitive to the changes in building density compared to building height because building density controls the roughness in cities. The negative contribution to SUHI followed the pattern: high-density regions > middle-density regions > low-density regions [Fig. 5(d)]. In particular, LPB exhibited the strongest contribution to weaken SUHI from the aspect of ΔT_{Con} , with a median value of approximately -0.9 K. This can be attributed to its lower resistance, allowing for more heat transfer from urban surface into near-surface air. Conversely, in the VEG, the boxplot consistently registers values above 0, indicating a positive contribution of ΔT_{Con} to SUHI. In this region, LST is much lower than that in UMBs, which means a lower temperature gradient over surface. Coupled with higher r_a due to denser vegetation foliage, less heat is released, contributing to the stabilization of LST.

The evapotranspiration term (ΔT_{Eva}) is highly aggregated in the core urban with dense low-rise buildings, which bears a close resemblance to the spatial distribution of ΔT_{AH} (Fig. 4). ΔT_{Eva} is a function of the Bowen ratio (β), which is particularly sensitive to land surface properties (e.g., land cover type and vegetation density). The urban regions, characterized by buildings and pavement, tend to have higher sensible heat fluxes and lower latent heat fluxes when compared to natural vegetation areas (Fig. 6). This is primarily due to their lower rates of evapotranspiration. Among UMBs, high-density regions contribute most significantly to SUHI intensity through ΔT_{Eva} , with LPB being particularly notable (nearly 5.5 K), followed by the middle- and low-density regions [Fig. 5(e)]. The impact of building height on this contribution is relatively less pronounced. In the VEG, ΔT_{Eva} contributes negatively to SUHI, as expected. This is attributed to increased shading, transpiration, and moisture availability in vegetation areas, resulting in a lower Bowen ratio when compared to impervious surfaces.

The spatial distribution of heat storage term (ΔT_{HS}) illustrated a tendency to increase from the core urban region

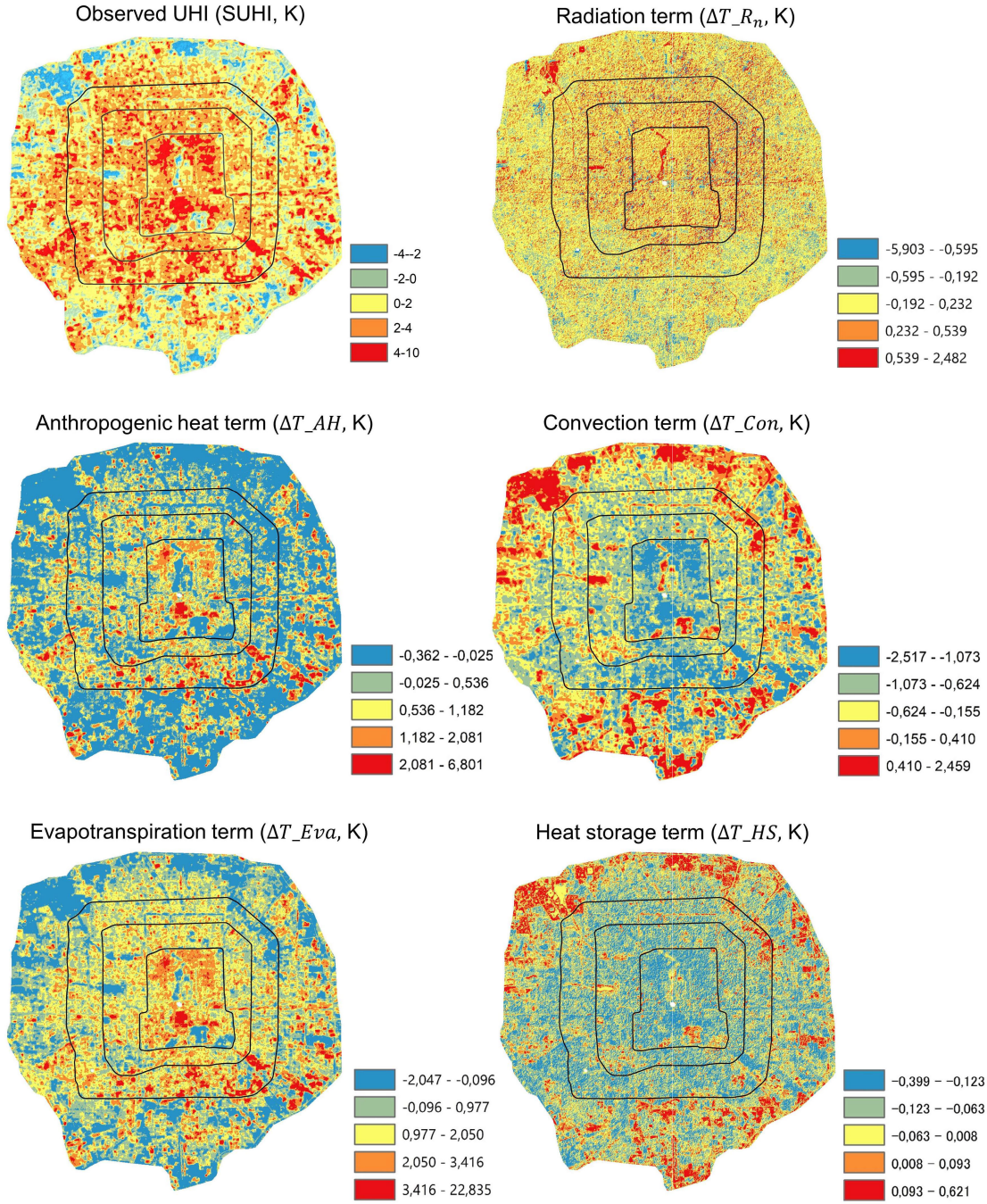


Fig. 4. Calculated SUHI intensity from Landsat 8 and decomposed SUHI contribution terms. The black line in each subfigure means the Ring Road.

toward the outskirts (Fig. 4). At the time of image acquisition, the surface temperature is higher than the subsurface soil temperature, resulting in downward heat transfer. This can contribute to a decrease in LST. The urban region displayed a larger heat storage capacity than the bare surface areas outside the urban region and the vegetation regions. This pattern explains why UMBs have negative, but vegetation regions had positive ΔT_{HS} values. As seen in Fig. 5(f), building density impacts the contribution of ΔT_{HS} on SUHI more than the building height, and however, the variations were relatively weak with median values among UMBs hovering around -0.1 K.

Fig. 5(g) shows that it is the variations in ΔT_{Eva} (associated with Bowen ratio or land surface type), rather than other terms, that control the SUHI intensity within UMBs and VEG. This tendency is strongly correlated with building density, especially in the LPB. In the high-density regions, the contribution of ΔT_{Eva} exceeds 1 K when compared to that in the low-density regions. For low-density regions, building height affects the contribution terms of SUHI intensity significantly, especially ΔT_{Eva} and ΔT_{Con} . Furthermore, ΔT_{Eva} , ΔT_{AH} , and ΔT_{R_n} have positive contributions on SUHI intensity, whereas ΔT_{Eva} and ΔT_{HS} play a negative role.

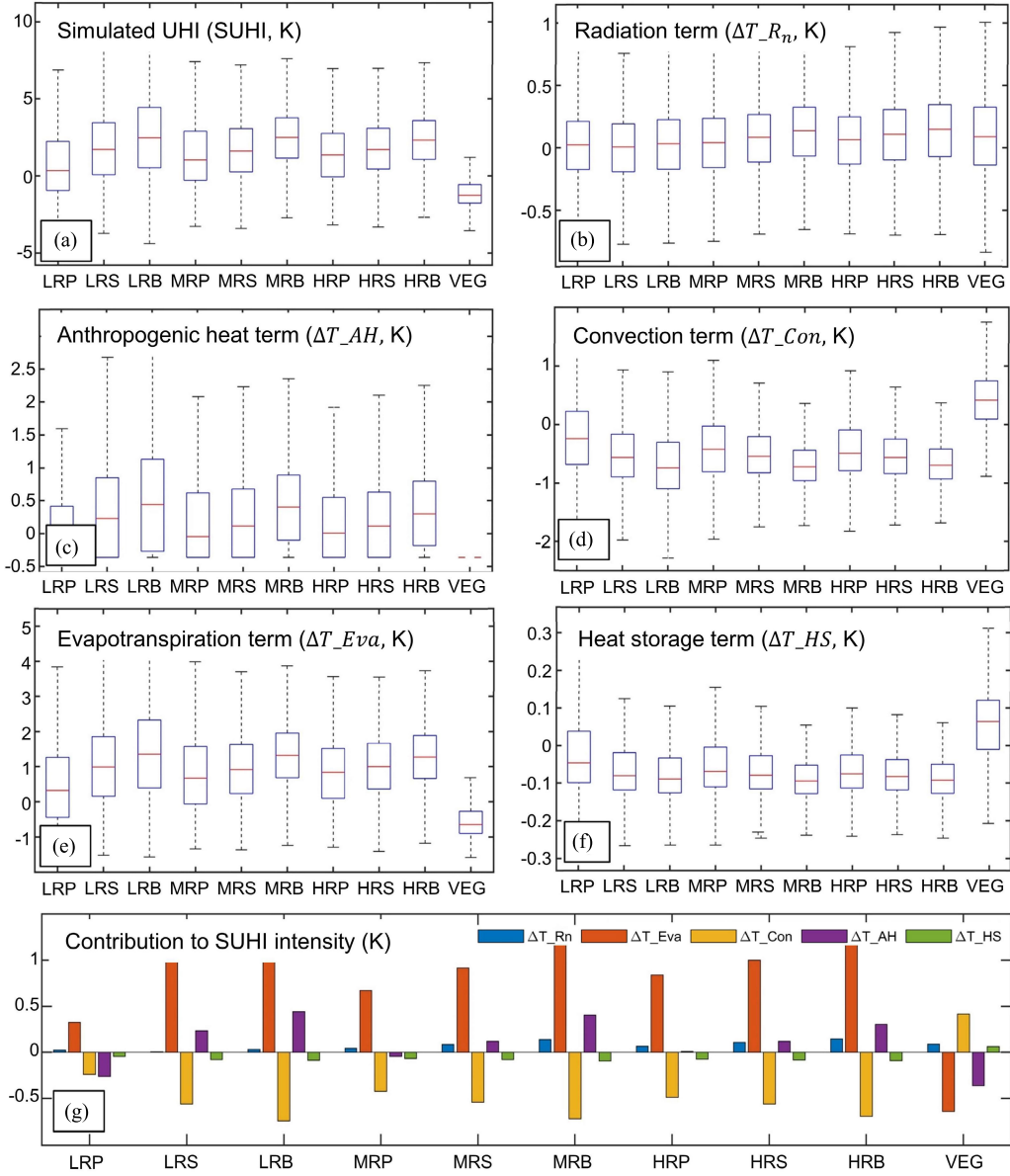


Fig. 5. (a) SUHI intensity and (b)–(f) each SUHI contribution term in different UMBs and VEG. (g) Average median values of each SUHI contribution term among various UMBs and VEG.

V. DISCUSSION

A. Implications for SUHI Mitigation

In the urban region of Beijing characterized by numerous buildings and impervious surface, it was observed that the evapotranspiration term (ΔT_{Eva}) had the largest contribution on the variations of SUHIs, supporting findings of [19] in part cities of North America. This highlights the importance of the capacity of urban surface to evaporate water in controlling SUHI intensity, rather than others such as the convection efficiency of heat transfer from surface to atmosphere, anthropogenic heat release, and heat storage. Among UMBs, building density notably influenced the variations in ΔT_{Eva} and ΔT_{AH} , with high-density regions contributing the most. Therefore, we recommend strategies aimed at reducing the Bowen ratio for SUHI mitigation. These strategies encompass

two aspects: first, increasing latent heat flux through measures such as implementing green roofs, green walls, and permeable materials; and second, decreasing sensible heat flux through practices such as open building arrangements and reduced building density over urban surfaces. The former is conducive to heat loss by evapotranspiration, while the latter can reduce heat retention. It should be noted that for an effective implementation of each strategy, one needs to balance all UHI contributions. For instance, open building arrangements can decrease the sensible heat flux but may increase net radiation. UHI decomposition algorithms provide a framework that allows to assess which effect is superior and, subsequently, which strategy is best suitable at the respective location.

The convection term (ΔT_{Con}) and heat storage term (ΔT_{HS}) both illustrated a negative contribution to SUHI

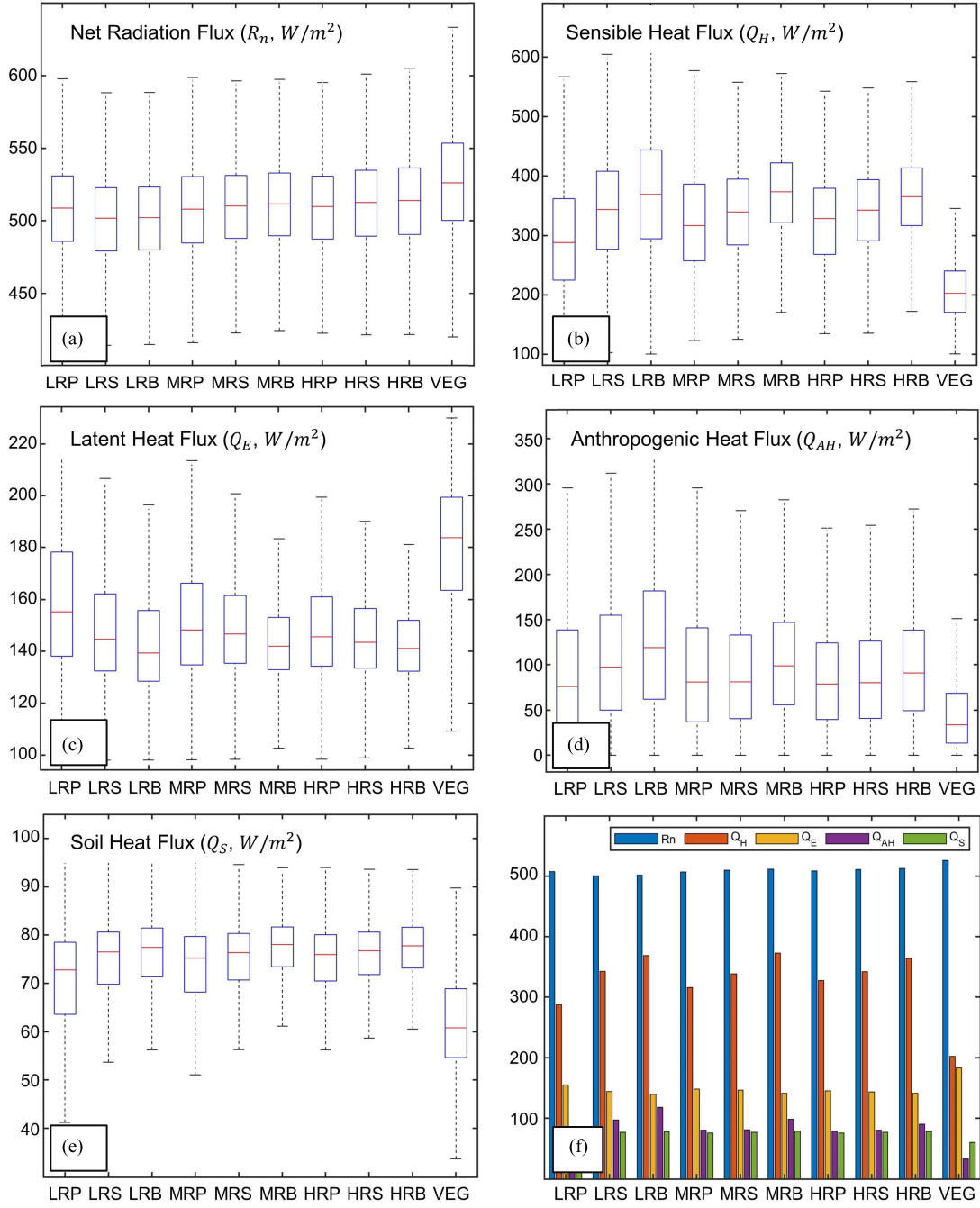


Fig. 6. (a)–(e) How each SEB flux changes with different UMBs and VEG. (f) Average median value of each SEB flux among various UMBs and VEG.

intensity, particularly within the UMBs. This is mainly caused by a higher LST than the lower temperatures in the atmosphere and soil, resulting in upward and downward heat transfer, ultimately leading to a reduction of LST. However, in urban regions, continuous solar radiation supplies the energy and heats the land surface, maintaining a relatively higher LST due to lower albedo [45]. In this case, strategies that aim to increase soil moisture such as irrigation and urban rivers are recommended. These measures serve a dual purpose: 1) they reduce soil temperature, thereby mitigating heat transfer into the subsurface and 2) they facilitate the removal of absorbed heat, preventing excess heat release at night.

B. Potential Applications of UHI Decomposition Method

The relative importance of five contribution terms to SUHI, as indicated in this study, is specific to a particular city and time. Indeed, these contributions vary with day/night, seasons, and regions [7], [19], [44]. The urban heat environment at night has a significant impact on human health (e.g., sleep disturbances and heat-related illnesses), energy consumption (e.g., heating/cooling of air conditioning), and air pollutants (e.g., greenhouse gas emissions) [9], [46], [47]. More importantly, the UHI contribution terms and their sensitivities to influencing factors, particularly urban morphological features, change within a 24-h cycle due to variations in

solar radiation intensity [48], [49]. Another point is that UHI contribution terms and their relative importance vary across cities in different climate zones. UHI mitigation and adaptation strategies need to be tailored to the specific characteristics of each climate zone [7], [19], [45]. For instance, strategies to reduce UHI effects in a humid tropical climate may differ from those in an arid climate. In addition, traditional LULC-based analysis is advantageous for analyzing the heating and cooling effects of specific surface coverages, but it hardly quantifies the local heat transfer process. The suggested IBM method can deal with this insufficiency, by estimating SEB fluxes and converting them into corresponding temperature changes. This provides a platform to balance all contributions for policymakers and urban planners, allowing them to devise more efficient measures (e.g., urban management and green infrastructure).

The application of this method is not limited to urban settings but extends to other fields, such as forests and wetlands. Taking forests as an example, the suggested method can be valuable to quantify the heating/cooling effects caused by forest fragmentation and deforestation, by assuming “urban region” as forest fragmented/deforested area and “rural region” as forest area. Such an application is crucial to estimate carbon storage, feedback loops, and biodiversity conservation [42]. In addition, a remote sensing-based method can significantly reduce the computational time and achieve good performance, compared to climate models and micrometeorological simulations. This offers a possible solution for analyzing the climate response and its driving mechanisms on a global scale, especially when combined with the application of GEE.

C. Limitations

1) *Resolution Issue:* We used the ERA5 dataset for supplying key meteorological parameters due to its global coverage and long-time data accessibility, but the resolution of this dataset is much coarser than Landsat 8. This means that ERA5 data cannot capture fine-scale variations in surface features that can affect aerodynamic resistance and heat fluxes, such as variations in land cover type, topography, and surface roughness. These uncertainties can affect the accuracy of models and simulations relying on these parameters, particularly in studies requiring high spatial and temporal resolution data for localized analysis. In the future, when using ERA5 data at a coarser resolution, there might be a need to interpolate the data to match the resolution of Landsat 8. In addition, although we resampled the Landsat 8 LST product to achieve a spatial resolution of 30 m for the calculated SEB fluxes and SUHI contribution terms, the resolution is still not enough for much more detailed analysis in highly heterogeneous regions. For example, the building shadow cannot be well displayed, which directly affects the estimate of radiation term ($\Delta T \cdot R_n$). For future work, we plan to explore the use of higher resolution remote sensing images (e.g., Sentinel and Gaofen satellites) or unmanned aerial vehicles.

2) *Accuracy Issue:* We evaluated the accuracy of anthropogenic heat flux, while others were not considered, due to the absence of meteorological stations data. Even though our result showed a well consistency with existing products, it is

imperative to conduct additional experiments, particularly in conjunction with flux towers, to further refine our assessments. The estimated Q_{AH} is a little lower than that of [26] because the remote sensing and SEB-based method to estimate Q_{AH} assumed that Q_{AH} contributes only to sensible heat flux and neglected the influence of other SEB terms. Another point is related to the definition of urban and rural boundaries. This study selected a 10-km buffer outside the urban boundary as a rural area. Different setups of buffer zones can lead to variations in UHI intensity [10], and the background information used for extracting SUHI contribution terms can also differ. For future work, we would compare two commonly employed methods for distinguishing urban and suburban areas: the buffer zone method and LULC-based method [25].

3) *Method Issue:* The convection and evapotranspiration term obtained using the IBM method is a function of aerodynamic resistance and Bowen ratio, respectively. This assumes that aerodynamic resistance is independent not only of Bowen ratio but also of the other three terms. However, existing literature has highlighted certain shortcomings in this method, including an overestimate of convection term and an underestimate of radiation and heat storage term [19]. These discrepancies together lead to an underestimate of simulated SUHI intensity when compared to reference values. In future, we would consider a two-resistance mechanism to replace the Bowen ratio by surface resistance for comparison with IBM.

VI. CONCLUSION

UHI is among the most pronounced human impacts on Earth, and a comprehensive understanding of the influencing mechanisms of UHI is necessary to formulate efficient adaptation and mitigation strategies. This study suggests an SEB-based approach to attribute SUHI intensity to various biophysical terms using remote sensing images and applies it in Beijing, one of the largest cities in the world. The results demonstrate good performance in comparison to SUHI intensity calculated from Landsat 8 LST product. In addition, the results highlight the importance of surface evaporating water, with the evapotranspiration term contributing the most to SUHI changes during summer. This phenomenon is particularly significant in low-rise, high-density blocks. The convection and heat storage term play a positive role in reducing SUHI intensity. The method suggested provides valuable insights into the driving mechanism of SUHI from heat formation and analyzes how they vary with different UMBs, which are crucial for developing locally adapted strategies of urban transformation, with a focus on heat management.

ACKNOWLEDGMENT

The ERA5 hourly atmospheric reanalysis dataset, Landsat 8 data, and SRTM elevation data are openly available at <https://developers.google.com/earth-engine/datasets/>, using codes:ee.ImageCollection("ECMWF/ERA5_LAND/HOURLY"), ee.ImageCollection("Landsat/LC08/C02/T1"), and ee.Image("USGS/SRTMGL1_003"), respectively. The CLCD product is available in the public domain at <https://doi.org/10.5281/zenodo.4417810>. The urban UMBs dataset is available from Beijing City Lab (<http://www.beijingcitylab.com>).

REFERENCES

- [1] E. Kalnay and M. Cai, "Impact of urbanization and land-use change on climate," *Nature*, vol. 423, no. 6939, pp. 528–531, May 2003, doi: [10.1038/nature01675](https://doi.org/10.1038/nature01675).
- [2] G. Manoli et al., "Magnitude of urban heat islands largely explained by climate and population," *Nature*, vol. 573, no. 7772, pp. 55–60, Sep. 2019, doi: [10.1038/s41586-019-1512-9](https://doi.org/10.1038/s41586-019-1512-9).
- [3] L. Mentaschi et al., "Global long-term mapping of surface temperature shows intensified intra-city urban heat island extremes," *Global Environ. Change*, vol. 72, Jan. 2022, Art. no. 102441, doi: [10.1016/j.gloenvcha.2021.102441](https://doi.org/10.1016/j.gloenvcha.2021.102441).
- [4] R. Basu, "High ambient temperature and mortality: A review of epidemiologic studies from 2001 to 2008," *Environ. Health*, vol. 8, no. 1, pp. 1–13, Dec. 2009, doi: [10.1186/1476-069x-8-40](https://doi.org/10.1186/1476-069x-8-40).
- [5] J. C. Fyfe, N. P. Gillett, and F. W. Zwiers, "Overestimated global warming over the past 20 years," *Nature Climate Change*, vol. 3, no. 9, pp. 767–769, Sep. 2013, doi: [10.1038/nclimate1972](https://doi.org/10.1038/nclimate1972).
- [6] J. Wang et al., "Anthropogenic emissions and urbanization increase risk of compound hot extremes in cities," *Nature Climate Change*, vol. 11, no. 12, pp. 1084–1089, Dec. 2021, doi: [10.1038/s41558-021-01196-2](https://doi.org/10.1038/s41558-021-01196-2).
- [7] L. Zhao, X. Lee, R. B. Smith, and K. Oleson, "Strong contributions of local background climate to urban heat islands," *Nature*, vol. 511, no. 7508, pp. 216–219, Jul. 2014, doi: [10.1038/nature13462](https://doi.org/10.1038/nature13462).
- [8] A. A. Scott, B. Zaitchik, D. W. Waugh, and K. O'Meara, "Intraurban temperature variability in Baltimore," *J. Appl. Meteorol. Climatol.*, vol. 56, no. 1, pp. 159–171, Jan. 2017, doi: [10.1175/jamc-d-16-0232.1](https://doi.org/10.1175/jamc-d-16-0232.1).
- [9] W.-B. Wu, Z.-W. Yu, J. Ma, and B. Zhao, "Quantifying the influence of 2D and 3D urban morphology on the thermal environment across climatic zones," *Landscape Urban Planning*, vol. 226, Oct. 2022, Art. no. 104499, doi: [10.1016/j.landurbplan.2022.104499](https://doi.org/10.1016/j.landurbplan.2022.104499).
- [10] S. Peng et al., "Surface urban heat island across 419 global big cities," *Environ. Sci. Technol.*, vol. 46, no. 2, pp. 696–703, Jan. 2012, doi: [10.1021/es2030438](https://doi.org/10.1021/es2030438).
- [11] C. R. D. Almeida, A. C. Teodoro, and A. Gonçalves, "Study of the Urban Heat Island (UHI) using remote sensing data/techniques: A systematic review," *Environments*, vol. 8, no. 10, p. 105, Oct. 2021, doi: [10.3390/environments8100105](https://doi.org/10.3390/environments8100105).
- [12] K. Deilami, M. Kamruzzaman, and Y. Liu, "Urban heat island effect: A systematic review of spatio-temporal factors, data, methods, and mitigation measures," *Int. J. Appl. Earth Observ. Geoinf.*, vol. 67, pp. 30–42, May 2018, doi: [10.1016/j.jag.2017.12.009](https://doi.org/10.1016/j.jag.2017.12.009).
- [13] H. Du et al., "Contrasting trends and drivers of global surface and canopy urban heat islands," *Geophys. Res. Lett.*, vol. 50, no. 15, Aug. 2023, doi: [10.1029/2023gl104661](https://doi.org/10.1029/2023gl104661).
- [14] P. Sismanidis, I. Keramitsoglou, and C. T. Kiranoudis, "A satellite-based system for continuous monitoring of surface urban heat islands," *Urban Climate*, vol. 14, pp. 141–153, Dec. 2015, doi: [10.1016/j.uclim.2015.06.001](https://doi.org/10.1016/j.uclim.2015.06.001).
- [15] X. Huang and Y. Wang, "Investigating the effects of 3D urban morphology on the surface urban heat island effect in urban functional zones by using high-resolution remote sensing data: A case study of Wuhan, Central China," *ISPRS J. Photogramm. Remote Sens.*, vol. 152, pp. 119–131, Jun. 2019, doi: [10.1016/j.isprsjprs.2019.04.010](https://doi.org/10.1016/j.isprsjprs.2019.04.010).
- [16] T. M. Logan, B. Zaitchik, S. Guikema, and A. Nisbet, "Night and day: The influence and relative importance of urban characteristics on remotely sensed Land Surface Temperature," *Remote Sens. Environ.*, vol. 247, Sep. 2020, Art. no. 111861, doi: [10.1016/j.rse.2020.111861](https://doi.org/10.1016/j.rse.2020.111861).
- [17] F. Guo, U. Schlink, W. Wu, D. Hu, and J. Sun, "Scale-dependent and season-dependent impacts of 2D/3D building morphology on Land Surface Temperature," *Sustain. Cities Soc.*, vol. 97, Oct. 2023, Art. no. 104788, doi: [10.1016/j.scs.2023.104788](https://doi.org/10.1016/j.scs.2023.104788).
- [18] D. Hertel and U. Schlink, "Decomposition of urban temperatures for targeted climate change adaptation," *Environ. Model. Softw.*, vol. 113, pp. 20–28, Mar. 2019, doi: [10.1016/j.envsoft.2018.11.015](https://doi.org/10.1016/j.envsoft.2018.11.015).
- [19] D. Li et al., "Urban heat island: Aerodynamics or imperviousness?" *Sci. Adv.*, vol. 5, no. 4, Apr. 2019, Art. no. eaau4299, doi: [10.1126/sciadv.aau4299](https://doi.org/10.1126/sciadv.aau4299).
- [20] T. R. Oke, "The urban energy balance," *Prog. Phys. Geography Earth Environ.*, vol. 12, no. 4, pp. 471–508, Dec. 1988, doi: [10.1177/030913338801200401](https://doi.org/10.1177/030913338801200401).
- [21] M. Mahour, V. Tolpekin, A. Stein, and A. Sharif, "A comparison of two downscaling procedures to increase the spatial resolution of mapping actual evapotranspiration," *ISPRS J. Photogramm. Remote Sens.*, vol. 126, pp. 56–67, Apr. 2017, doi: [10.1016/j.isprsjprs.2017.02.004](https://doi.org/10.1016/j.isprsjprs.2017.02.004).
- [22] M. Rahimzadegan and A. Janani, "Estimating evapotranspiration of pistachio crop based on SEBAL algorithm using Landsat 8 satellite imagery," *Agricul. Water Manag.*, vol. 217, pp. 383–390, May 2019, doi: [10.1016/j.agwat.2019.03.018](https://doi.org/10.1016/j.agwat.2019.03.018).
- [23] L. Laipelt et al., "Long-term monitoring of evapotranspiration using the SEBAL algorithm and Google Earth engine cloud computing," *ISPRS J. Photogramm. Remote Sens.*, vol. 178, pp. 81–96, Aug. 2021, doi: [10.1016/j.isprsjprs.2021.05.018](https://doi.org/10.1016/j.isprsjprs.2021.05.018).
- [24] H. E. Beck, N. E. Zimmermann, T. R. McVicar, N. Vergopolan, A. Berg, and E. F. Wood, "Present and future Köppen-geiger climate classification maps at 1-km resolution," *Sci. Data*, vol. 5, no. 1, pp. 1–12, Oct. 2018, doi: [10.1038/sdata.2018.214](https://doi.org/10.1038/sdata.2018.214).
- [25] Q. Meng, L. Zhang, Z. Sun, F. Meng, L. Wang, and Y. Sun, "Characterizing spatial and temporal trends of surface urban heat island effect in an urban main built-up area: A 12-year case study in Beijing, China," *Remote Sens. Environ.*, vol. 204, pp. 826–837, Jan. 2018, doi: [10.1016/j.rse.2017.09.019](https://doi.org/10.1016/j.rse.2017.09.019).
- [26] Q. Meng et al., "Anthropogenic heat variation during the COVID-19 pandemic control measures in four Chinese megacities," *Remote Sens. Environ.*, vol. 293, Aug. 2023, Art. no. 113602, doi: [10.1016/j.rse.2023.113602](https://doi.org/10.1016/j.rse.2023.113602).
- [27] F. Guo, D. Hu, and U. Schlink, "A new nonlinear method for downscaling Land Surface Temperature by integrating guided and Gaussian filtering," *Remote Sens. Environ.*, vol. 271, Mar. 2022, Art. no. 112915, doi: [10.1016/j.rse.2022.112915](https://doi.org/10.1016/j.rse.2022.112915).
- [28] H. H. Jaafar and F. A. Ahmad, "Time series trends of Landsat-based ET using automated calibration in METRIC and SEBAL: The bekaa valley, Lebanon," *Remote Sens. Environ.*, vol. 238, Mar. 2020, Art. no. 111034, doi: [10.1016/j.rse.2018.12.033](https://doi.org/10.1016/j.rse.2018.12.033).
- [29] J. M. Sabater, "ERA5-land hourly data from 1981 to present, Copernicus climate change service (C3S) climate data store (CDS)[data set]," Tech. Rep., 2019. [Online]. Available: <https://cds.climate.copernicus.eu/cdsapp#!/dataset/10.24381/cds.e2161bac?tab=overview>, doi: [10.24381/cds.e2161bac](https://doi.org/10.24381/cds.e2161bac).
- [30] X. Liu and Y. Long, "Automated identification and characterization of parcels with OpenStreetMap and points of interest," *Environ. Planning B, Planning Des.*, vol. 43, no. 2, pp. 341–360, Mar. 2016, doi: [10.1177/0265813515604767](https://doi.org/10.1177/0265813515604767).
- [31] D. Hu et al., "How do urban morphological blocks shape spatial patterns of Land Surface Temperature over different seasons? A multifactorial driving analysis of Beijing, China," *Int. J. Appl. Earth Observ. Geoinf.*, vol. 106, Feb. 2022, Art. no. 102648, doi: [10.1016/j.jag.2021.102648](https://doi.org/10.1016/j.jag.2021.102648).
- [32] J. Yang and X. Huang, "The 30 m annual land cover dataset and its dynamics in China from 1990 to 2019," *Earth Syst. Sci. Data*, vol. 13, no. 8, pp. 3907–3925, Aug. 2021, doi: [10.5194/essd-13-3907-2021](https://doi.org/10.5194/essd-13-3907-2021).
- [33] R. G. Allen, "Using the FAO-56 dual crop coefficient method over an irrigated region as part of an evapotranspiration intercomparison study," *J. Hydrol.*, vol. 229, nos. 1–2, pp. 27–41, Mar. 2000, doi: [10.1016/S0022-1694\(99\)00194-8](https://doi.org/10.1016/S0022-1694(99)00194-8).
- [34] S. D. Chakraborty, Y. Kant, and D. Mitra, "Assessment of Land Surface Temperature and heat fluxes over Delhi using remote sensing data," *J. Environ. Manag.*, vol. 148, pp. 143–152, Jan. 2015, doi: [10.1016/j.jenvman.2013.11.034](https://doi.org/10.1016/j.jenvman.2013.11.034).
- [35] R. Allen, M. Tasumi, R. Trezza, R. Waters, and W. Bastiaanssen, "SEBAL (surface energy balance algorithms for land)-advanced training and users manual-Idaho implementation (version 1.0)," The Idaho Dept. Water Resour., Boise, ID, USA, Tech. Rep., 2002. [Online]. Available: <https://posmet.ufv.br/wp-content/uploads/2017/04/MET-479-Waters-et-al-SEBAL.pdf>
- [36] W. G. M. Bastiaanssen, M. Menenti, R. Trezza, R. Waters, and A. A. M. Holtslag, "A remote sensing surface energy balance algorithm for land (SEBAL). 1. Formulation," *J. Hydrol.*, vols. 212–213, pp. 198–212, Dec. 1998, doi: [10.1016/S0022-1694\(98\)00253-4](https://doi.org/10.1016/S0022-1694(98)00253-4).
- [37] J. Monteith and M. Unsworth, *Principles of Environmental Physics: Plants, Animals, and The Atmosphere*. Cambridge, MA, USA: Academic Press, 2013.
- [38] W. G. M. Bastiaanssen, "SEBAL-based sensible and latent heat fluxes in the irrigated Gediz basin, Turkey," *J. Hydrol.*, vol. 229, nos. 1–2, pp. 87–100, Mar. 2000, doi: [10.1016/S0022-1694\(99\)00202-4](https://doi.org/10.1016/S0022-1694(99)00202-4).
- [39] S. Kato and Y. Yamaguchi, "Analysis of urban heat-island effect using ASTER and ETM+ data: Separation of anthropogenic heat discharge and natural heat radiation from sensible heat flux," *Remote Sens. Environ.*, vol. 99, nos. 1–2, pp. 44–54, Nov. 2005, doi: [10.1016/j.rse.2005.04.026](https://doi.org/10.1016/j.rse.2005.04.026).

- [40] J. Qian, Q. Meng, L. Zhang, D. Hu, X. Hu, and W. Liu, "Improved anthropogenic heat flux model for fine spatiotemporal information in Southeast China," *Environ. Pollut.*, vol. 299, Apr. 2022, Art. no. 118917, doi: [10.1016/j.envpol.2022.118917](https://doi.org/10.1016/j.envpol.2022.118917).
- [41] C. Berger, J. Rosentreter, M. Voltersen, C. Baumgart, C. Schmulius, and S. Hese, "Spatio-temporal analysis of the relationship between 2D/3D urban site characteristics and Land Surface Temperature," *Remote Sens. Environ.*, vol. 193, pp. 225–243, May 2017, doi: [10.1016/j.rse.2017.02.020](https://doi.org/10.1016/j.rse.2017.02.020).
- [42] X. Lee et al., "Observed increase in local cooling effect of deforestation at higher latitudes," *Nature*, vol. 479, no. 7373, pp. 384–387, Nov. 2011, doi: [10.1038/nature10588](https://doi.org/10.1038/nature10588).
- [43] G. Roe, "Feedbacks, timescales, and seeing red," *Annu. Rev. Earth Planet. Sci.*, vol. 37, no. 1, pp. 93–115, May 2009, doi: [10.1146/annurev.earth.061008.134734](https://doi.org/10.1146/annurev.earth.061008.134734).
- [44] D. Hertel and U. Schlink, "Entropy frameworks for urban heat storage can support targeted adaptation strategies," *Urban Climate*, vol. 42, Mar. 2022, Art. no. 101129, doi: [10.1016/j.uclim.2022.101129](https://doi.org/10.1016/j.uclim.2022.101129).
- [45] F. Guo, U. Schlink, W. Wu, D. Hu, and J. Sun, "A new framework quantifying the effect of morphological features on urban temperatures," *Sustain. Cities Soc.*, vol. 99, Dec. 2023, Art. no. 104923, doi: [10.1016/j.scs.2023.104923](https://doi.org/10.1016/j.scs.2023.104923).
- [46] F. Salamanca, M. Georgescu, A. Mahalov, M. Moustaqi, and M. Wang, "Anthropogenic heating of the urban environment due to air conditioning," *J. Geophys. Res., Atmos.*, vol. 119, no. 10, pp. 5949–5965, May 2014, doi: [10.1002/2013jd021225](https://doi.org/10.1002/2013jd021225).
- [47] F. Guo, Q. Wu, and U. Schlink, "3D building configuration as the driver of diurnal and nocturnal Land Surface Temperatures: Application in Beijing's old city," *Building Environ.*, vol. 206, Dec. 2021, Art. no. 108354, doi: [10.1016/j.buildenv.2021.108354](https://doi.org/10.1016/j.buildenv.2021.108354).
- [48] Y. Chang et al., "Exploring diurnal thermal variations in urban local climate zones with ECOSTRESS Land Surface Temperature data," *Remote Sens. Environ.*, vol. 263, Sep. 2021, Art. no. 112544, doi: [10.1016/j.rse.2021.112544](https://doi.org/10.1016/j.rse.2021.112544).
- [49] D. Zhou, J. Xiao, S. Frolking, L. Zhang, and G. Zhou, "Urbanization contributes little to global warming but substantially intensifies local and regional land surface warming," *Earth's Future*, vol. 10, no. 5, May 2022, Art. no. e2021EF002401, doi: [10.1029/2021ef002401](https://doi.org/10.1029/2021ef002401).



Fengxiang Guo received the B.S. degree in surveying and mapping engineering and the M.S. degree in geodesy and surveying engineering from Jilin University, Changchun, China, in 2015 and 2018, respectively. He is currently pursuing the Ph.D. degree in geography with the Helmholtz-Centre for Environmental Research—UFZ, Leipzig, Germany.

His research methodology focuses on monitoring urban dynamics in 3-D space as well as urban microclimate using remote sensing technology. A focal point is to understand how urban morphology, particularly the built forms, affects the land surface temperature across scales, seasons, and cities. Related studies include land surface temperature downscaling, surface energy balance, 3-D urban morphological indicators design, and a large-scale comparison of urban morphology across countries.

- Daniel Hertel** received the B.Sc. and M.Sc. degrees in meteorology from the Leipzig Institute for Meteorology, University of Leipzig, Leipzig, Germany, in 2012 and 2015, respectively, and the Dr.rer.nat. degree (magna cum laude) from the University of Leipzig, supported by the Helmholtz-Centre for Environmental Research—UFZ, Leipzig, in 2022. He was a Deutsche Bundesstiftung Umwelt (DBU), Osnabrück, Doctoral Scholarship Program Fellow from 2015 to 2019. From January 2022 to May 2023, he worked as a Scientific Employee in a DBU-funded project about heat stress on the neighborhood scale using the planetary health approach. He is currently working as a Post-Doctoral Researcher with the Helmholtz Climate Initiative (HI-CAM) Project, phase 2 with the Helmholtz-Centre for Environmental Research—UFZ. His main research interests include urban climatology, urban climate modeling, heat attribution in urban areas, planetary health, and climate adaptation measures against local heat stress.



Jiangkang Qian received the B.Sc. degree from the School of Geosciences, Yunnan University, Kunming, China, in 2020. He is currently pursuing the Ph.D. degree with the Aerospace Information Research Institute, Chinese Academy of Sciences, Beijing, China.

His research interests include the quantification of anthropogenic heat emission and the analysis and simulation of driving factors in urban thermal environments.



Uwe Schlink received the diploma degree in theoretical physics from the Technical University of Dresden, Dresden, Germany, in 1985, and the Dr.rer.nat. and Dr.habil. degrees in meteorology from the University of Leipzig, Leipzig, Germany, in 1995 and 2003, respectively. He works with the Helmholtz Centre for Environmental Research (UFZ), Leipzig, where he heads the Urban Climate and Personal Exposure working group, Department of Urban and Environmental Sociology. He has been teaching applied meteorology and advanced statistical data analysis at the University of Leipzig since 2004. He is an Adjunct Faculty with the Department of Civil Engineering, Indian Institute of Technology Madras (IITM), Chennai, India, and a fellow of the Institute of Advanced Studies, Durham University, Durham, U.K. His research interests include urban climate research, deterministic and statistical modeling, Bayesian inference, person-based measurements using wearable sensors, and adaptation to extreme urban environmental conditions such as heat and air pollution.



Die Hu received the B.S. degree in geographic information science from the China University of Geosciences, Beijing, China, in 2017, and the Ph.D. degree in cartography and geographic information systems from the University of Chinese Academy of Sciences, Beijing, in 2022.

She is currently a Post-Doctoral Fellow with the Department of Physical Geography, College of Urban and Environmental Sciences, Peking University, Beijing. Her research focuses on urban environmental remote sensing, especially on spatial and temporal patterns, driving mechanisms, and downscaling modeling of urban land surface temperature.



Jiangkang Qian received the B.Sc. degree from the School of Geosciences, Yunnan University, Kunming, China, in 2020. He is currently pursuing the Ph.D. degree with the Aerospace Information Research Institute, Chinese Academy of Sciences, Beijing, China.

His research interests include the quantification of anthropogenic heat emission and the analysis and simulation of driving factors in urban thermal environments.



Wanben Wu was born in Tongling, China, in August 15, 1994. He received the Ph.D. degree from the School of Life and Sciences, Fudan University, Shanghai, China, in 2023.

He currently serves as a Post-Doctoral Researcher with the Center for Ecological Dynamics in a Novel Biosphere (ECONOVO), Aarhus University, Aarhus, Denmark. His research delves into the realm of geospatial big data, where he explores ecosystem responses and underlying mechanisms triggered by rewilding in Europe. His passion lies in unraveling intricate human–nature dynamics, and his expertise extends to diverse areas, including the mapping of urban form, urban heat exposure studies, and in-depth investigations into forest functions.